Journal Pre-proof

Rapid and Selective Targeting of Heterogeneous Pancreatic Neuroendocrine Tumors

G. Kate Park, Jeong Heon Lee, Eduardo Soriano, Myunghwan Choi, Kai Bao, Wataru Katagiri, Do-Yeon Kim, Ji-Hye Paik, Seok-Hyun Yun, John V. Frangioni, Thomas E. Clancy, Satoshi Kashiwagi, Maged Henary, Hak Soo Choi

PII: S2589-0042(20)30190-5

DOI: https://doi.org/10.1016/j.isci.2020.101006

Reference: ISCI 101006

To appear in: *ISCIENCE*

Received Date: 2 September 2019

Revised Date: 10 February 2020

Accepted Date: 18 March 2020

Please cite this article as: Park, G.K., Lee, J.H., Soriano, E., Choi, M., Bao, K., Katagiri, W., Kim, D.-Y., Paik, J.-H., Yun, S.-H., Frangioni, J.V., Clancy, T.E., Kashiwagi, S., Henary, M., Choi, H.S., Rapid and Selective Targeting of Heterogeneous Pancreatic Neuroendocrine Tumors, *ISCIENCE* (2020), doi: https://doi.org/10.1016/j.isci.2020.101006.

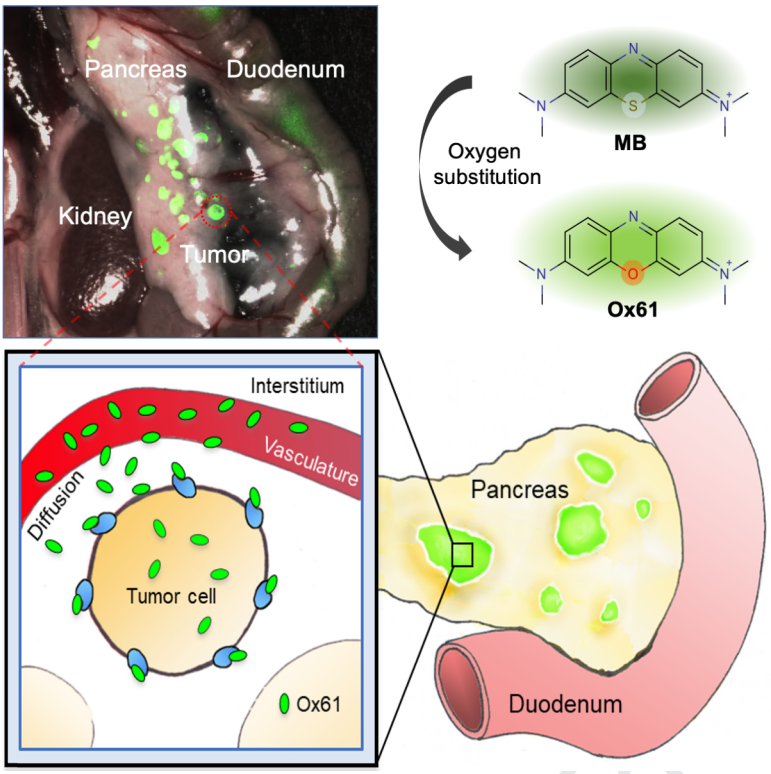

Rapid and Selective Targeting of Heterogeneous Pancreatic Neuroendocrine Tumors

G. Kate Park[1]*, Jeong Heon Lee[1]*, Eduardo Soriano[2], Myunghwan Choi[3], Kai Bao[1], Wataru Katagiri[1], Do-Yeon Kim[4], Ji-Hye Paik[4], Seok-Hyun Yun[3], John V. Frangioni[5], Thomas E. Clancy[6], Satoshi Kashiwagi[1], Maged Henary[2**], and Hak Soo Choi[1, 7**]

*These authors contributed equally to this work.

[1]Gordon Center for Medical Imaging, Department of Radiology, Massachusetts General Hospital and Harvard Medical School, Boston, MA 02114

[2]Department of Chemistry, Georgia State University, Atlanta, GA 30303

[3]Wellman Center for Photomedicine, Massachusetts General Hospital and Harvard Medical School, MA 02139

[4]Department of Pathology and Laboratory Medicine, Weill Cornell Medical College, New York, NY 10065

[5]Curadel, LLC, Marlborough, MA 01752

[6]Division of Surgical Oncology, Brigham and Women's Hospital and Dana-Farber Cancer Institute, Boston, MA 02215

[7]Lead Contact

**Corresponding Authors: H.S.C. hchoi12@mgh.harvard.edu or M.H. mhenary1@gsu.edu

Running Head: Image-Guided Drug Delivery to PNET

Key Words: Near-infrared fluorescence, targeted fluorophore, tumor targeting, image-guided surgery, pancreatic neuroendocrine tumor

Word Count: 3029 (exclusive of Abstract, Methods, References and Figure legends)

SUMMARY

Design of tissue-specific contrast agents to delineate tumors from background tissues is a major unmet clinical need for ultimate surgical interventions. Bioconjugation of fluorophore(s) to a ligand has been mainly used to target overexpressed receptors on tumors. However, the size of the final targeted ligand can be large >20 kDa and cannot readily cross the microvasculature to meet the specific tissue, resulting in low targetability with a high background. Here, we report a small and hydrophilic phenoxazine with high targetability and retention to pancreatic neuroendocrine tumor. This bioengineered fluorophore permits sensitive detection of ultrasmall (<0.5 mm) ectopic tumors within a few seconds after a single bolus injection, highlighting every tumor in the pancreas from the surrounding healthy tissues with reasonable half-life. The knowledge-based approach and validation used to develop structure-inherent tumor targeted fluorophores have a tremendous potential to improve treatment outcome by providing definite tumor margins for image-guided surgery.

Word Count: 149 Words (150 max)

INTRODUCTION

An ideal tumor-targeted contrast agent should have high uptake and prolonged retention in malignant tissue as well as minimum uptake and fast clearance from surrounding normal tissues (Choi and Kim, 2020, Owens et al., 2015). The most common tumor targeting strategy is to conjugate a targeting ligand (e.g., small molecule, peptide, peptidomimetic, or protein) to a contrast agent (Choi et al., 2013). Targeted delivery of a specific agent to the cancerous tissue is significant for oncologists to plan a treatment strategy as well as for surgeons to decide the surgical margin based on image-guidance (Kang et al., 2016, Kang et al., 2020).

The resection of pancreatic neuroendocrine tumor (PNET) and the avoidance of normal pancreas represent a significant unmet clinical need. Currently, intraoperative visual inspection and palpation performed by the surgeon is considered the most reliable source for PNET detection which often results in incomplete resection of the tumor, with 5 years-disease recurrence rate of 10% and 97% of patients without and with liver metastasis, respectively (Mayo et al., 2010, Lo et al., 1997, Mabrut et al., 2001, Ravi and Britton, 2007). Therefore, complete tumor resection remains the only treatment option that improves patient survival (Wong et al., 2018, Mayo et al., 2010).

Significant efforts have been focused on improving preoperative and intraoperative identification of tumors and their margins, however, it presents a major challenge to detect PNET with sufficient sensitivity (Grant, 2005, Galiber et al., 1988). Conventional preoperative techniques such as computed tomography (CT), magnetic resonance imaging (MRI), and endoscopic ultrasonography are successful in localizing larger tumors, though detection is very challenging for subcentimeter lesions with a broad-ranged sensitivity (9.6 - 71%) (Galiber et al., 1988). Undetectable small size PNET can cause severe symptoms of hormonal imbalance such as hypoglycemia or hyperglucagonemia due to excess production of insulin or glucagon, respectively. To increase small tumor detection, glucagon-like peptide-1 (GLP-1) radioligands were developed to diagnose PNET with highly expressed GLP-1 receptors on beta-cells, yet detecting tumors <2 cm remains elusive (Reiner et al., 2011, Wild et al., 2008).

Near-infrared (NIR) fluorescence imaging has the potential to improve the detectability and spatial resolution significantly (Hyun et al., 2015b, Hyun et al., 2014, Owens et al., 2016). Currently, only two small NIR fluorophores, methylene blue (MB) and indocyanine green (ICG), have been FDA-approved for tumor imaging in the clinics without clarifying the mode of action (Tummers et al., 2014, Alander et al., 2012), resulting in low tumor-to-background ratio (TBR)[17,18]. Previously, MB was used for detecting insulinoma, the

most common functioning PNET, using optical imaging (Winer et al., 2010). However, due to its poor optical properties (i.e., low molecular brightness), rapid clearance from the body, and chemical reduction, MB is not ideal for intraoperative tumor targeting. Therefore, bioengineering of a single NIR small fluorophore to target such a tiny neoplasm is of significant importance with improved specificity and biodistribution (Hyun et al., 2015a, Choi, 2014).

The delivery and retention of a molecule in tumor tissue is dependent on the size, charge, hydrophobicity, pharmacodynamics, pharmacokinetics and its transport across the tumor vasculature (Kang et al., 2018, Lee et al., 2012a). However, the physicochemical properties of cancer-targeting fluorophores are not well established. In the present study, we have developed a lead PNET-targeted, phenoxazine-based NIR fluorescent contrast agent by analyzing the biodistribution of a small fluorophore library with the potentials to accumulate into PNET using insulinoma-bearing transgenic mice. Thereby, we have determined bioengineering of the physicochemical properties and pharmacokinetics is required to achieve the specific targeting for PNET that can provide image-guidance needed during the tumor resection.

RESULTS

Systemic Modification for Development of PNET Targeting NIR Fluorophore. MB is the first and the only NIR fluorophore used for intraoperative localization of PNET (Winer et al., 2010). However, when MB is administrated intravenously into the body, approximately 75% is reduced to Leuco-MB in erythrocytes via the endogenous reductase by consuming NADPH and loses fluorescence (May et al., 2003, Blazquez-Castro et al., 2009, Bradberry, 2003, Matsui et al., 2010). Despite these limitations of MB as an endocrine tumor imaging agent, we still believed that the core structure of the MB holds the key properties for the initial accumulation into the tumor and hypothesized that systematic modification of MB could potentially improve its optical and biological characteristics.

Therefore, we first focused on enhancement of optical properties and *in vivo* stability of MB. Among several different substitutions of the MB core (data not shown), we found that substitution of the sulfur atom of MB with oxygen resulted in the most improvement in both optical and biological properties (**Figure 1A).** With this first modification, we named the molecule Ox61 (see **Transparent Methods** and **Figures S1-S5**). The single oxygen substitution in Ox61 led to hypsochromic shift and 5.7-fold brightness increase compared to MB: 1.3-fold increase in molecular absorbance ($\Delta\varepsilon$ = 12,300 $M^{-1}cm^{-1}$) and 4.5-fold increase in quantum yield ($\Delta\Phi$ = 8.6%), respectively (**Figures 1B-1D**) (Bradberry, 2003).

To show high redox stability towards biological reduction after oxygen substitution, we performed an *in vitro* live cell assay to evaluate the cellular specificity by comparing MB and Ox61 in NIT-1 (pancreatic β-cell). Both MB and Ox61 stained the NIT-1 cells, however, Ox61 showed a significantly higher signal compared to MB (**Figure 1E**, P <0.05). We subsequently treated the membrane-stained cells with 0.1 mM periodic acid to test the presence of the leuco form of both fluorophores. Interestingly, the fluorescence signal of MB inside NIT-1 cells was recovered by oxidation, while no notable changes were observed in the Ox61 stained cells, which remained high pre- and post-treatment. Similarly, we also treated periodic acid on the kidneys resected from normal CD-1 mice 1 h after injecting 1.5 mg/kg of MB or Ox61 intravenously. The fluorescence signal significantly increased in the MB-injected mouse kidney, while no intensity changes were found in the Ox61-injected mouse kidney (**Figure S6**, P <0.0001). This indicates that MB is reduced to LMB by endogenous reductase, but Ox61 is stable from the redox cycle and retains strong fluorescence signal.

Structural Characterization of PNET Targeting NIR Fluorophore. After the first modification and the improvement in optical properties and biological stability, we then synthesized 18 additional phenoxazine derivatives by varying side chains (**Figure 2A**). To test the tumor targetability of these derivatives, 1.5 mg/kg of each molecule was injected intravenously into the insulinoma bearing mice and imaged 30 min after injection under the FLARE intraoperative optical imaging system (**Figure S7A**) (Gioux et al., 2010). Physicochemical properties and tumor-to-background ratio (Tu/Pa) of MB and molecules in PNET-library are summarized in **Table 1**. Among the 19 contrast agents, four (Ox61, 89, 261, and 266) had TBR >2.0 and only Ox61 had TBR >5.0. We then analyzed the quantitative physicochemical properties of the molecules to define the criteria required for PNET targetability. Molecular weight (MW), hydrophobicity, and total polar surface area of each agent were plotted in a chart and Ox61 was labeled with red (TBR >5.0), MB with blue, molecules with TBR above 2 with orange and the rest with dark grey (**Figure 2B**). Based on the chart, we were able to determines the PNET targetability range for each chemical property (red margin) and if the molecule did not fall within the optimal range, it had low or no tumor targetability. In summary, highly hydrophilic molecules with low molecular weight (<300 Da), and low TPSA (<40) had suitable accumulation in PNET. In addition, positive charge of the molecule favored tumor accumulation. Another interesting observation was that change in hydrophobicity of the molecule with elongation of side chain dramatically altered tumor targetability (**Figure S7B**). Other critical factors influencing tumor-targeting are the plasma pharmacokinetics of probe residence in the circulation and diffusivity of the molecule across tumor vasculature into the extravascular tissue[25,26,] (Dewhirst and Secomb, 2017). To evaluate the probe transport in circulation, we performed plasma protein binding test using the rapid equilibrium dialysis (RED) to determine the free (%Fu) and bound (%Bound) fraction of drugs in plasma. As a result, Ox61 with the highest tumor uptake had the least plasma protein bound fraction (45% bound) and the Ox89, 261, and 266 with TBR around 2 also had (<50 - 70% bound), which is relatively low compared to the rest of drugs with low or no tumor uptake (90% - 100% bound) (**Table 1, Figure 2B**). These results indicate that low plasma binding favors tumor targeting, which would prevent sequestration of a probe to plasma compartment.

Kinetics and Dose Dependence of Ox61. Since MB is the only available PNET contrast agent, we compared results directly obtained with the lead compound Ox61 with MB. We first compared *in vivo* biodistribution and clearance pattern in normal CD-1 mice 4 h after a

single intravenous injection of Ox61 or MB (**Figure S8**). The pattern for biodistribution and renal excretion was almost identical, but the fluorescence signal in the Ox61 injected mice was about 2-5-fold higher than MB injected mice. We also compared *in vivo* biodistribution and blood clearance and found that Ox61 had prolonged blood circulation compared with MB. In these comparisons, we excluded the measurement of leuco-MB form to make a direct comparison with Ox61 for their *in vivo* fluorescence signals. The elimination blood half-life ($t_{1/2\beta}$) of Ox61 was 3-fold longer than that of MB (47 vs. 15 min) in mice (**Figure 3A**). We next performed a wide range dose test between 0.3 to 6.0 mg/kg. Although the lowest dose of 0.3 mg/kg resulted in improved TBR compared to MB, substantial signal increase in tumors occurred with 1.5 mg/kg and 3.0 mg/kg of Ox61, which showed much higher TBR compared with MB (**Figure 3B**, P <0.001). Tumor signals were further increased when injected with the maximum dose of 6.0 mg/kg, but the background signal in pancreas also increased, which lowered the TBR between 1 h to 4 h. To determine the optimum time-point for tumor targeting, we injected 1.5 mg/kg of Ox61 or MB into insulinoma-bearing mice and observed the TBR change over 4 h post-injection. In both cases, tumors became bright immediately after injection (**Figure 3C**). However, the pattern of uptake and retention at the tumorous tissue was notably different between Ox61 and MB. Ox61 gradually accumulated into insulinomas over 3 h post-injection, whereas MB rapidly disappeared within 1 h. The peak TBR of Ox61 occur 3-4 h post-intravenous injection, at which point surrounding background signal had decreased drastically.

Tumor Targetability and Specificity of Ox61. Having determined optimal kinetics and dose, we tested the effect of physiological changes from tumor developmental stage on Ox61 uptake and retention. Small occult PNET (<2 mm) are extremely difficult to localize and cannot typically be visualized in the surgical field. When insulinoma-bearing mice were injected with Ox61, however, small occult tumors were clearly visualized throughout the pancreas (**Supplemental Video S1**). In contrast, similar tumors were not detectable at 4 h post-injection of MB because of its fast elimination, leuco-MB formation, and poor optical properties (**Figure 3D**). After a single intravenous injection of Ox61, we successfully resected 5 different developmental stages of tumorigenesis under fluorescence image guidance with high TBR (tumor to pancreas) (**Figure 3E**). Since MRI has been used previously to monitor tumor growth, we compared tumor detectability with intraoperative fluorescence imaging. MRI visualized both hyperintense (early stage) and isointense (late stage) of larger sized tumors (>2 mm) of 13 wk old insulinoma mouse, yet delineating tumor

margins was a challenge. After injection of 1.5 mg/kg of Ox61 into the same mouse, we obtained intraoperative fluorescence images co-registered with the MR images (**Figure S9A**). Dual-modality imaging permitted clearer margin assessment, however, fluorescence imaging revealed additional small tumors that were not detectable by MRI.

Next, we tested the effect of physiological change in tumor stages on Ox61 accumulation. PNET stages are well defined in transgenic mice: pre-angiogenic/hyperplasia (5-6 wk), angiogenic/dysplasia (7-9 wk), early stage tumors (10-11 wk), mature stage tumors (11-13 wk), and necrotic tumors (>13 wk) (Bergers et al., 1999). We performed Ox61-based tumor imaging in 5 to 13 wk old insulinoma-bearing mice (**Figure S9B**). Surprisingly, Ox61 was able to target and localize pre-angiogenic tumors in mice with a reliable TBR $\geq$ 2.0 but short retention time compared to angiogenic and tumor stage. Histopathologic evaluation was performed on resected tumor tissues confirmed the morphological changes of tumors at each stage (**Figure 3F**). Despite the heterogeneity nature of pancreatic endocrine tumorigenesis, the efficient uptake of Ox61 at all stages of tumors were observed. Hyperplasia stage and angiogenic stage tissues showed homogenous fluorescence signal at the tumor site, while Ox61 uptake in the late stage of PNET were heterogeneous because, presumably, of limited blood supply. Areas around open vasculature exhibited more favorable accumulation of Ox61 compared to other areas with compressed vasculature (arrowheads).

Physiological Mechanism of Action of Ox61. To better understand the physiological mechanism of Ox61 accumulation at the tumor site, we measured absolute fluorescence intensity at the pancreas and the tumor from 0 to 150 seconds post-injection of 1.5 mg/kg of Ox61 and corresponding images at 4 different time points on the graph (**Figure 4A**). The entire pancreas and its associated tumors were stained with high intensity immediately after the injection. Both pancreas and tumors showed decrease in signal after reaching the peak of the blood distribution phase (phase 2). Interestingly, the signal intensity in the tumor increased gradually after a short period of clearance while the pancreas signal continued to decrease (phase 3-4). This phenomenon clearly demonstrates the high specificity of Ox61 to tumor site. The distribution of tumor-targeting probe is dependent on the transport through tumor vasculature into the extravascular tissue[27,28,] (Dewhirst and Secomb, 2017). For the further analysis of the diffusion of the Ox61 from the tumor capillaries, we performed real-time, quantitative intravital fluorescence imaging. Within 10 sec, after the injection a large amount of Ox61 diffused from microvasculature of the tumor followed by rapid accumulation

in all tumorous tissues as well as large venules (**Figure 4B**). We next compared the performance of Ox61 to various tumor specific protein-conjugated fluorophores (GLP-1, cRGDyK and CREKA micelle, see **Transparent Methods**), which are known to have high specificity to tumors (Choi et al., 2013, Wild et al., 2008, Ruoslahti et al., 2010). None of these conjugates were able to target a single tumor in insulinoma-bearing mice 1 h post-injection (**Figure S10A**). In addition, we tested tumor cell specificity of Ox61 by generating NIT-1 subcutaneous tumor in nude mice and injected with 1.5 mg/kg of Ox61 but were not able to observe accumulation into the tumor (**Figure S10B**).

DISCUSSION

We have successfully developed a pancreatic tumor-targeted contrast agent, Ox61, through systemic engineering of a clinically available, yet poorly performing NIR fluorophore, MB, for intraoperative imaging (Winer et al., 2010, Matsui et al., 2010). Ox61 has overcome historical shortcomings of NIR fluorophores including low water solubility, short circulation time, low quantum efficiencies, poor photostability, high plasma protein binding rate, and low TBR (Choi and Frangioni, 2010). Ox61 has improved molecular brightness (> 5-fold), redox stability, blood circulation (> 3-fold), and targeting specificity (> 10-fold) compared with MB. The improvement in optical properties resulted from 1) high oscillator strength derived from the larger atom size (covalent radius of atom: S = 0.104 nm vs. O = 0.066 nm), 2) low energy π-π^* transition donating electron density (electronegativity: S = 2.4 vs. O = 3.5), and 3) low solvation energies in polar media (HBA: S = 2 vs. O = 3) (Bradberry, 2003).

Our data clearly indicate that design of a tumor-targeting fluorophore requires a specific combination of physicochemical properties of the molecule. By analyzing quantitative physicochemical properties of synthesized molecules (**Figure 2A**), we have determined that specificity to tumor is highly dependent on the chemical structure, MW, hydrophilicity (log*D* at pH 7.4), and total polar surface charge (**Figure S8**) (Lee et al., 2012b). Molecular weight was critical property because molecules larger than 300 Da had poor targetability. Hydrophilicity of molecule also played important role in determining tumor specificity, for example elongation of one or two methyl group on the side chain increased log*D* and decreased the tumor targetability. These physicochemical properties had combinatorial effect on the tumor targetability. MW less than 300 Da did not always have good tumor targetability if it also had high log*D* (Ox4). Also, if the molecule had slightly high log*D* with low TPSA and MW (Ox89), it likely also displayed good tumor targetability.

The distribution of tumor-targeting agents also relies on the plasma pharmacokinetics and transport through tumor vasculature into the extravascular tumor tissue. (Dewhirst and Secomb, 2017) Plasma protein binding (PPB) greatly impacts the behavior (distribution and elimination) of the drug, where only the unbound fraction is available to interact with the target site. (Trainor, 2007) To have lasting pharmacological effect, a large fraction of the drug must be distributed to the tumorous tissue with high affinity (Dewhirst and Secomb, 2017). Interestingly, Ox61 had the highest unbound fraction compared to all the other drugs in the library. In addition, molecules with similar physicochemical properties as Ox61 but lower TBR had smaller unbound fraction compared with Ox61. This clearly explained why

Ox61 outperformed all the other drugs and emphasize that PPB is a critical parameter to determine the availability of drug to the biological target.

Our data clearly show that Ox61 quickly extravasated and accumulated into tumor tissue with higher affinity compared with normal pancreas after intravenous injection (**Figure 4**). Physicochemical and pharmacodynamic characteristics including positive charge of Ox61 might facilitated extravasation and accumulation in tumor tissue with the negative charges of the vessel luminal face and molecules in the interstitial space (Campbell et al., 2002, Azzi et al., 2013). The development of targeted NIR fluorescent contrast agents for endocrine tumor is particularly difficult because it requires initial distribution into the endocrine organ while simultaneously localize in higher concentration within the targeting tumor, regardless of anatomic location and barriers to give contrast between the normal tissue (Hyun et al., 2015b, Hyun et al., 2014, Owens et al., 2016). When bioengineering contrast agents which target tumors by their inherent chemical structures, we must determine the design criteria (i.e. size, charge and hydrophobicity) of the drug with regards to the plasma pharmacokinetics and physiological barriers to the target tissue. A significant portion of Ox61 injected intravenously in a single formulation was immediately delivered to the tumors, providing unparalleled contrast between the normal pancreas and the pancreatic tumor. To our knowledge, there is no single contrast agent that can highlight tumor within a minute after intravenous injection.

In conclusion, NIR fluorescent intraoperative imaging using Ox61 greatly facilitated the localization of small occult PNET and has the potential to reduce operation times and increase the likelihood of negative margins. Our new technology of drug design for delivering targeted agent can be applied for developing various other tumor targeting agents (i.e., ovarian, breast, thyroid) and can result in immediate detection of tumor upon injection with high specificity, which is difficult to achieve with nanoparticles or proteins and transporter targeting. Furthermore, Ox61 has high potential for accelerated approval by FDA for clinical use of tumor targeting, following the safety and regulatory guideline of MB.

Limitation of the Study: Even though we performed extensive in vivo and molecular analyses to determine to the mechanism of action allowing PNET targeting by Ox61, we were unable to determine target proteins or transporters on PNET cells. The physicochemical properties of Ox61 led rapid molecular distribution into the tumor site, whereas the retention mechanism on the target needs further investigation.

METHODS

All methods can be found in the accompanying Transparent Methods supplemental file.

ACKNOWLEDGMENTS

We thank Ivey Choi and Matt Laramie for manuscript editing. This study was supported by NIH grants NIBIB #R01EB011523 and #R01EB022230, and the Georgia Research Alliance for the Ventures Phase 1 Grant. This work was also supported by the Joint Research Project for Outstanding Research Institutions funded by the Gimhae Industry Promotion and Biomedical Foundation, the Health Technology R&D Project #HI19C0166 funded by the Ministry of Health & Welfare, South Korea. The content expressed is solely the responsibility of the authors and do not necessarily represent the official views of the NIH.

AUTHOR CONTRIBUTIONS

GKP, JHL, SK, ES, KB, MC, WK, and DYK, performed the experiments. GKP, JHL, SK, SHY, JHP, JVF, MH, and HSC reviewed, analyzed, and interpreted the data. GKP, JHL, SK, SHY, JHP, JVF, TEC, MH, and HSC wrote the paper. All authors discussed the results and commented on the manuscript.

DECLARATION OF INTERESTS

Dr. Frangioni is currently CEO of Curadel, LLC, a for-profit company that has licensed FLARE technology from Beth Israel Deaconess Medical Center.

TABLES AND FIGURES

Table 1. *In silico* physicochemical properties of PNET-targeted contrast agents.

Drug	MW (g/mol)	Log D (pH = 7.4)	TPSA ($Å^2$)	HBA	Volume ($Å^3$)	Dipole (debye)	Polarizability ($Cm^2\ V^{-1}$)	Plasma (% bound)	Tumor intensity
MB	284.40	-0.62	18.61	2	387.92	9.48	32.74	81.92	+++
Ox61	268.34	-1.09	27.84	3	382.04	9.38	30.34	45.87	+++++
Ox89	282.37	0.41	38.8	3	414.96	10.39	32.18	66.59	+++
Ox261	296.39	-0.38	27.84	3	447.63	8.24	34.03	65.82	+++
Ox266	294.38	-0.27	27.84	3	420.29	7.97	33.3	52.01	+++
Ox4	296.40	0.7	47.59	3	442.88	10.87	33.95	68.84	++
Ox14	318.40	0.51	59.21	3	449.6	9.66	36.39	96.42	++
Ox17	379.39	0.71	63.31	4	442.36	10.46	35.57	95.06	++
Ox94	324.45	1.66	47.59	3	504.25	7.79	37.64	82.91	++
Ox12	304.37	0.09	59.21	3	416.51	10.37	34.55	94.22	+
Ox116	334.40	-0.06	68.44	4	434.52	11.43	37.06	97.73	+
Ox117	348.43	0.91	56.82	4	499.17	10.22	38.9	86.13	+
Ox170	332.43	1.65	47.59	3	483.61	8.64	38.24	96.92	+
Ox269	308.40	0.18	27.84	3	447.78	7	35.14	81.28	+
Ox13	320.37	1.15	79.44	4	427.66	9.8	35.14	88.98	-
Ox16	334.40	1.62	70.65	4	460.05	12.8	37.06	87.62	-
Ox27	456.54	1.38	114.02	7	631.86	11.87	47.3	95.48	-
Ox37	450.17	0.63	123.25	6	606.75	22.07	46	73.12	-
Ox34	450.45	1.05	114.73	7	604.36	11.9	45.08	82.91	-
Ox96	324.45	0.33	27.84	3	508.56	74.72	37.72	81.45	-

MW, molecular weight; TPSA, total polar surface area; HBA, hydrogen bond acceptors. Tumor to background ratio (TBR) against normal pancreas was quantified and labeled as −, < 1; +, 1-2; ++, 2-3; +++, 3-4; +++++, > 5.

Figure Legends

Figure 1 PNET-specific fluorescent agents MB and Ox61. (**A)** Schematic drawing of PNET targeting by NIR fluorophores: MB converts to colorless leucomethylene blue (LMB) in erythrocytes, while oxygen substation become inert from redox mechanisms in the body. (**B)** Comparison of optical properties: Absorbance (solid line: left axis) and fluorescence emission (dotted line: right axis) spectra (**C)** optical properties measured in 100% serum, pH 7.0. (**D)** Fluorescence imaging of difference concentration of MB and Ox61 **e,** Live cell binding assay: 2 μM of MB or Ox61 was incubated for 1 h with NIT-1 (pancreatic beta cell) and α-TC1 (pancreatic alpha cell) cell lines, followed by treatment with 0.1 mM of periodic acid to induce oxidation. Scale bar = 50 μm.

Figure 2 PNET-specific fluorescent small molecule library. (**A)** Molecular structure of PNET-specific fluorophores **(B)** Quantitative calculation of molecular weight (MW), log*D*, TPSA, and plasma protein %Bound.

Figure 3 Intraoperative imaging and image-guided resection of PNET. (A) Blood half-life (%ID/g) of each compound in mice was calculated using the nonlinear regression two-phase exponential decay method (**B)** Dose-response curve of TBR (mean ± SEM) for MB (blue) and Ox61 (red). Different doses of each fluorophore were injected intravenously into insulinoma mice, and TBR (Tu/Pa) was quantified. (**C)** Quantitative time course assessment of TBR (mean ± SEM) for MB (blue) and Ox61 (red) for 4 h after a single bolus injection (1.5 mg/kg) of each fluorophore. (**D)** 1.5 mg/kg of MB or Ox61 was injected into age 14 wk insulinoma-bearing mice 4 h prior to imaging. Shown are occult and ectopic tumor metastases using NIR fluorescence. (**E)** Image-guided tumor resection after intraoperative tumor imaging and tumors at each stage were resected 4 h post-injection of Ox61 (1.5 mg/kg) and quantified (n = 5, mean ± s.d.). All NIR fluorescence images for each condition have identical exposure times and normalizations. Scale bars = 1 mm. (**F)** Histological evaluation of different stages of tumors in insulinoma-bearing pancreas. Shown are H&E and 700 nm NIR fluorescence (Ox61) of three different stages of resected tumors. Insulinoma stage of tumor showed presence of normal (arrow) and squeezed (arrowhead) vasculature. All NIR fluorescence images for each condition have identical exposure times and normalizations. I, insulinoma; E, exocrine pancreas. Scale bars = 100 μm

Figure 4 Extravasation and tumor uptake of Ox61 across tumor microvasculature. (**A)** Kinetics and representative intraoperative images for signal uptake in pancreas and PNET: 1) Pre-injection, 2) circulation, 3) initial uptake, and 4) accumulation and retention. Abbreviations used are In, intestine; Ki, kidneys; and Pa, pancreas. (**B)** Representative intravital microscopic images with real-time quantification of the extravasation rate after a single intravenous injection of Ox61. Microvasculature was labeled with FITC-dextran (green color) 10 min prior to intravenous injection of Ox61 (red color). White dotted circles indicate PNET; scale bar = 200 µm.

Supplementary Video S1. Real-time intraoperative imaging of insulinomas using Ox61 for 2 min post-injection, Related to Figure 3.

REFERENCES

Alander, J. T., Kaartinen, I., Laakso, A., Patila, T., Spillmann, T., Tuchin, V. V., Venermo, M. & Valisuo, P. 2012. A review of indocyanine green fluorescent imaging in surgery. *Int J Biomed Imaging,* 2012**,** 940585.

Azzi, S., Hebda, J. K. & Gavard, J. 2013. Vascular permeability and drug delivery in cancers. *Front Oncol,* 3**,** 211.

Bergers, G., Javaherian, K., Lo, K. M., Folkman, J. & Hanahan, D. 1999. Effects of angiogenesis inhibitors on multistage carcinogenesis in mice. *Science,* 284**,** 808-12.

Blazquez-Castro, A., Stockert, J. C., Sanz-Rodriguez, F., Zamarron, A. & Juarranz, A. 2009. Differential photodynamic response of cultured cells to methylene blue and toluidine blue: role of dark redox processes. *Photochem. Photobiol. Sci.,* 8**,** 371-6.

Bradberry, S. M. 2003. Occupational methaemoglobinaemia. Mechanisms of production, features, diagnosis and management including the use of methylene blue. *Toxicol. Rev.,* 22**,** 13-27.

Campbell, R. B., Fukumura, D., Brown, E. B., Mazzola, L. M., Izumi, Y., Jain, R. K., Torchilin, V. P. & Munn, L. L. 2002. Cationic charge determines the distribution of liposomes between the vascular and extravascular compartments of tumors. *Cancer Res,* 62**,** 6831-6.

Choi, H. S. 2014. Nanoparticle assembly: building blocks for tumour delivery. *Nature nanotechnology,* 9**,** 93-4.

Choi, H. S. & Frangioni, J. V. 2010. Nanoparticles for biomedical imaging: fundamentals of clinical translation. *Mol. Imaging,* 9**,** 291-310.

Choi, H. S., Gibbs, S. L., Lee, J. H., Kim, S. H., Ashitate, Y., Liu, F., Hyun, H., Park, G., Xie, Y., Bae, S., Henary, M. & Frangioni, J. V. 2013. Targeted zwitterionic near-infrared fluorophores for improved optical imaging. *Nat. Biotechnol.,* 31**,** 148-53.

Choi, H. S. & Kim, H. K. 2020. Multispectral image-guided surgery in patients. *Nat Biomed Eng,* 4**,** 245-6.

Dewhirst, M. W. & Secomb, T. W. 2017. Transport of drugs from blood vessels to tumour tissue. *Nat Rev Cancer,* 17**,** 738-750.

Galiber, A. K., Reading, C. C., Charboneau, J. W., Sheedy, P. F., 2nd, James, E. M., Gorman, B., Grant, C. S., Van Heerden, J. A. & Telander, R. L. 1988. Localization of pancreatic insulinoma: comparison of pre- and intraoperative US with CT and angiography. *Radiology,* 166**,** 405-8.

Gioux, S., Choi, H. S. & Frangioni, J. V. 2010. Image-guided surgery using invisible near-infrared light: fundamentals of clinical translation. *Mol. Imaging,* 9**,** 237-55.

Grant, C. S. 2005. Insulinoma. *Best Pract. Res. Clin. Gastroenterol.,* 19**,** 783-98.

Hyun, H., Park, M. H., Owens, E. A., Wada, H., Henary, M., Handgraaf, H. J., Vahrmeijer, A. L., Frangioni, J. V. & Choi, H. S. 2015a. Structure-inherent targeting of near-infrared fluorophores for parathyroid and thyroid gland imaging. *Nat Med,* 21**,** 192-7.

Hyun, H., Park, M. H., Owens, E. A., Wada, H., Henary, M., Handgraaf, H. J. M., Vahrmeijer, A. L., Frangioni, J. V. & Choi, H. S. 2015b. Structure-inherent targeting of NIR fluorophores for parathyroid and thyroid gland imaging. *Nat. Med.* , In press.

Hyun, H., Wada, H., K., B., Gravier, J., Yadav, Y., Laramie, M., Henary, M., Frangioni, J. V. & Choi, H. S. 2014. Phosphonated near-infrared fluorophores for biomedical imaging of bone. *Angew. Chem. Int. Ed.* , 53**,** 10668-10672.

Kang, H., Gravier, J., Bao, K., Wada, H., Lee, J. H., Baek, Y., El Fakhri, G., Gioux, S., Rubin, B. P., Coll, J. L. & Choi, H. S. 2016. Renal Clearable Organic Nanocarriers for Bioimaging and Drug Delivery. *Adv Mater,* 28**,** 8162-8168.

Kang, H., Hu, S., Cho, M. H., Hong, S. H., Choi, Y. & Choi, H. S. 2018. Theranostic Nanosystems for Targeted Cancer Therapy. *Nano Today,* 23**,** 59-72.

Kang, H., Stiles, W. R., Baek, Y., Nomura, S., Bao, K., Hu, S., Park, G. K., Jo, M. J., I, H., Coll, J. L., Rubin, B. P. & Choi, H. S. 2020. Renal Clearable Theranostic Nanoplatforms for Gastrointestinal Stromal Tumors. *Adv Mater,* 32**,** e1905899.

Lee, J. H., Park, G., Hong, G. H., Choi, J. & Choi, H. S. 2012a. Design considerations for targeted optical contrast agents. *Quantitative imaging in medicine and surgery,* 2**,** 266-73.

Lee, J. H., Park, G., Hong, G. H., Choi, J. & Choi, H. S. 2012b. Design considerations for targeted optical contrast agents. *Quant. Imaging Med. Surg.,* 2**,** 266-73.

Lo, C. Y., Lam, K. Y., Kung, A. W., Lam, K. S., Tung, P. H. & Fan, S. T. 1997. Pancreatic insulinomas. A 15-year experience. *Arch. Surg.,* 132**,** 926-30.

Mabrut, J. Y., Lifante, J. C., Cherki, S., Sin, S., Berger, N. & Peix, J. L. 2001. [Is preoperative localization of insulinomas necessary?]. *Ann. Chir.,* 126**,** 850-6.

Matsui, A., Tanaka, E., Choi, H. S., Kianzad, V., Gioux, S., Lomnes, S. J. & Frangioni, J. V. 2010. Real-time, near-infrared, fluorescence-guided identification of the ureters using methylene blue. *Surgery,* 148**,** 78-86.

May, J. M., Qu, Z. C. & Whitesell, R. R. 2003. Generation of oxidant stress in cultured endothelial cells by methylene blue: protective effects of glucose and ascorbic acid. *Biochem Pharmacol,* 66**,** 777-84.

Mayo, S. C., De Jong, M. C., Pulitano, C., Clary, B. M., Reddy, S. K., Gamblin, T. C., Celinksi, S. A., Kooby, D. A., Staley, C. A., Stokes, J. B., Chu, C. K., Ferrero, A., Schulick, R. D., Choti, M. A., Mentha, G., Strub, J., Bauer, T. W., Adams, R. B., Aldrighetti, L., Capussotti, L. & Pawlik, T. M. 2010. Surgical management of hepatic neuroendocrine tumor metastasis: results from an international multi-institutional analysis. *Ann Surg Oncol,* 17**,** 3129-36.

Owens, E. A., Henary, M., El Fakhri, G. & Choi, H. S. 2016. Tissue-Specific Near-Infrared Fluorescence Imaging. *Acc Chem Res,* 49**,** 1731-40.

Owens, E. A., Lee, S., Choi, J., Henary, M. & Choi, H. S. 2015. NIR fluorescent small molecules for intraoperative imaging. *Wiley Interdiscip Rev Nanomed Nanobiotechnol,* 7**,** 828-38.

Ravi, K. & Britton, B. J. 2007. Surgical approach to insulinomas: are pre-operative localisation tests necessary? *Ann. R. Coll. Surg. Engl.,* 89**,** 212-7.

Reiner, T., Thurber, G., Gaglia, J., Vinegoni, C., Liew, C. W., Upadhyay, R., Kohler, R. H., Li, L., Kulkarni, R. N., Benoist, C., Mathis, D. & Weissleder, R. 2011. Accurate measurement of pancreatic islet beta-cell mass using a second-generation fluorescent exendin-4 analog. *Proc. Natl. Acad. Sci. U. S. A.,* 108**,** 12815-20.

Ruoslahti, E., Bhatia, S. N. & Sailor, M. J. 2010. Targeting of drugs and nanoparticles to tumors. *J. Cell. Biol.,* 188**,** 759-68.

Trainor, G. L. 2007. The importance of plasma protein binding in drug discovery. *Expert Opin Drug Discov,* 2**,** 51-64.

Tummers, Q. R., Verbeek, F. P., Schaafsma, B. E., Boonstra, M. C., Van Der Vorst, J. R., Liefers, G. J., Van De Velde, C. J., Frangioni, J. V. & Vahrmeijer, A. L. 2014. Real-time intraoperative detection of breast cancer using near-infrared fluorescence imaging and Methylene Blue. *Eur J Surg Oncol,* 40**,** 850-8.

Wild, D., Macke, H., Christ, E., Gloor, B. & Reubi, J. C. 2008. Glucagon-like peptide 1-receptor scans to localize occult insulinomas. *N. Engl. J. Med.,* 359**,** 766-8.

Winer, J. H., Choi, H. S., Gibbs-Strauss, S. L., Ashitate, Y., Colson, Y. L. & Frangioni, J. V. 2010. Intraoperative localization of insulinoma and normal pancreas using invisible near-infrared fluorescent light. *Ann. Surg. Oncol.,* 17**,** 1094-100.

Wong, K. P., Tsang, J. S. & Lang, B. H. 2018. Role of surgery in pancreatic neuroendocrine tumor. *Gland Surg,* 7**,** 36-41.

A

Chemical modification

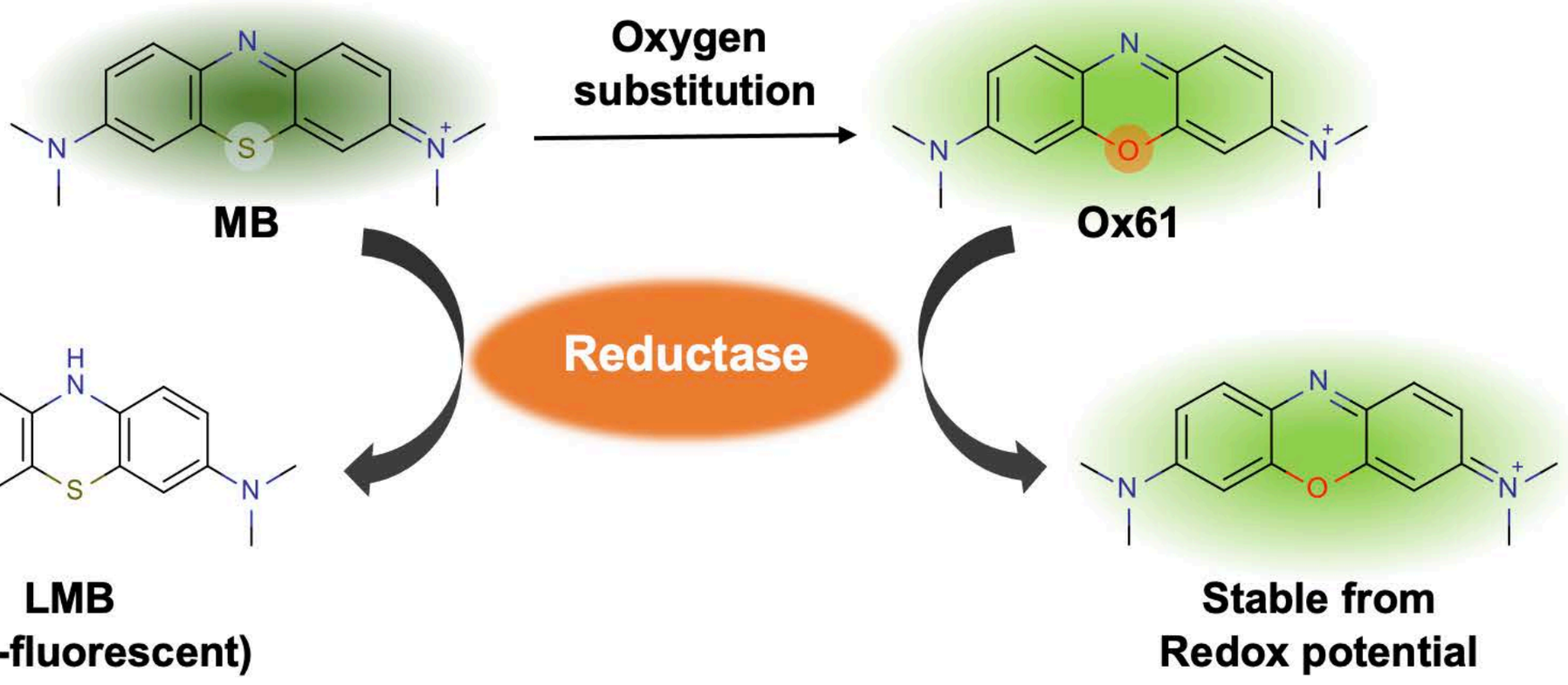

In vivo tumor targetability

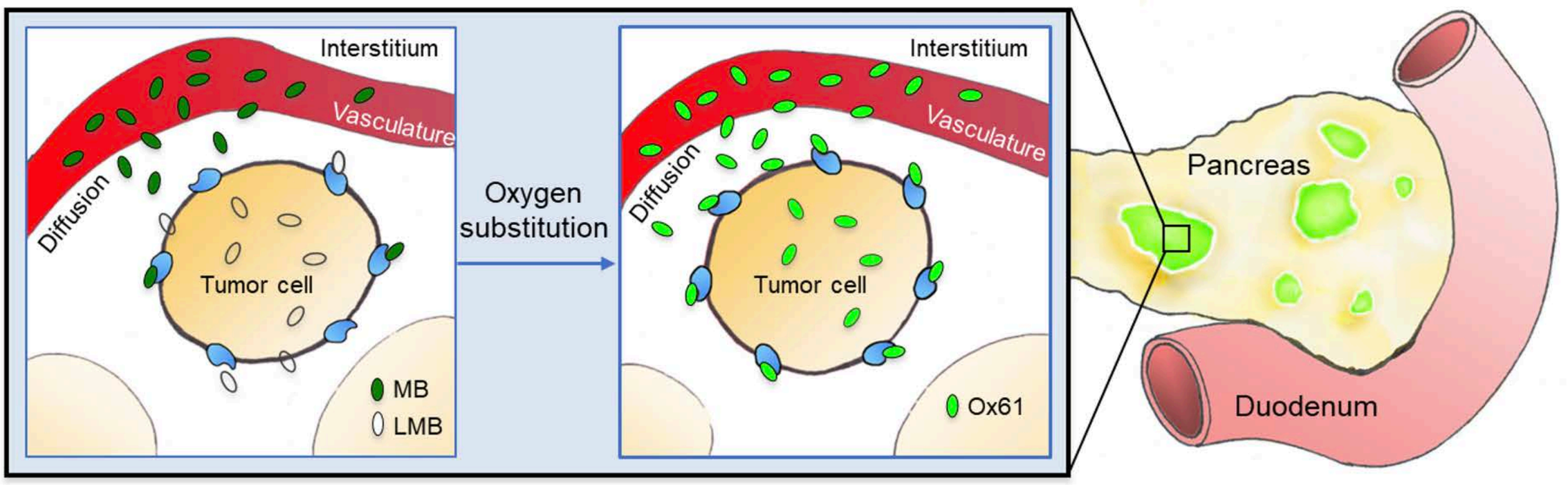

B

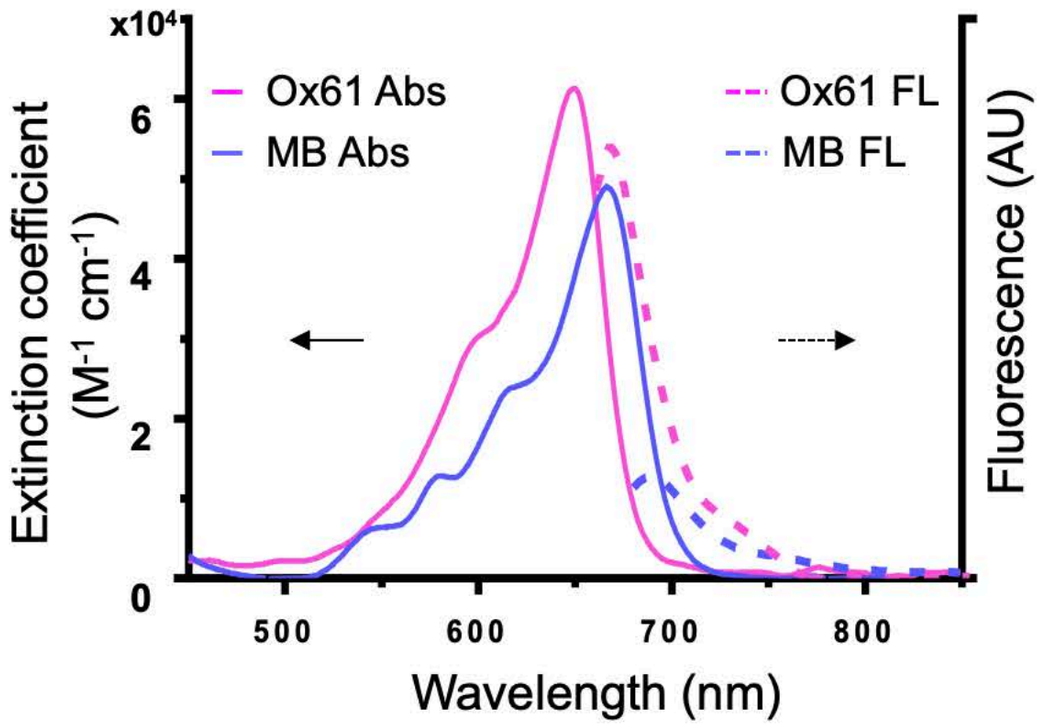

C

Optical property	Ox61	MB
Absorbance maximum (λ_{abs}, nm)	648	667
Emission maximum (λ_{em}, nm)	668	686
Stokes shift (nm)	20	19
Extinction coefficient (ε, $M^{-1}cm^{-1}$)	61,800	49,500
Quantum yield at 655 nm (Φ, %)	17.30	3.82
Molecular brightness ($\varepsilon x \Phi$, $M^{-1}cm^{-1}$)	10,691	1,891

D

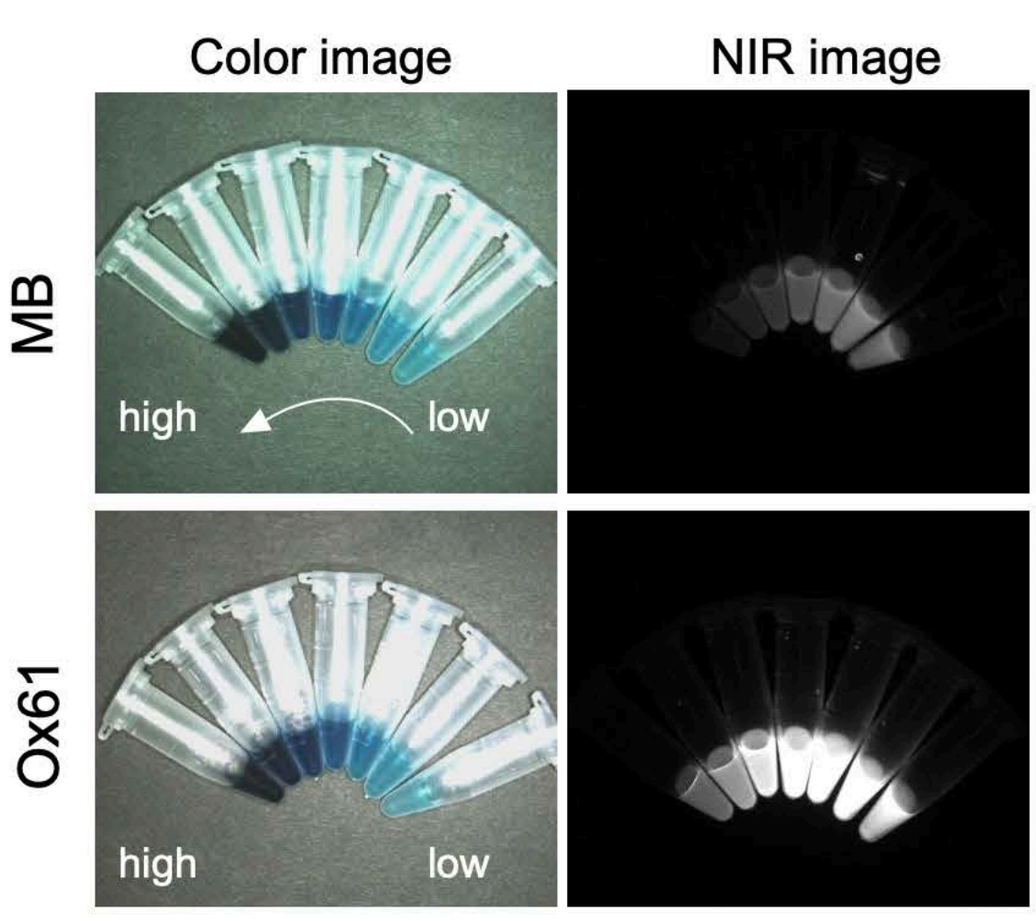

E

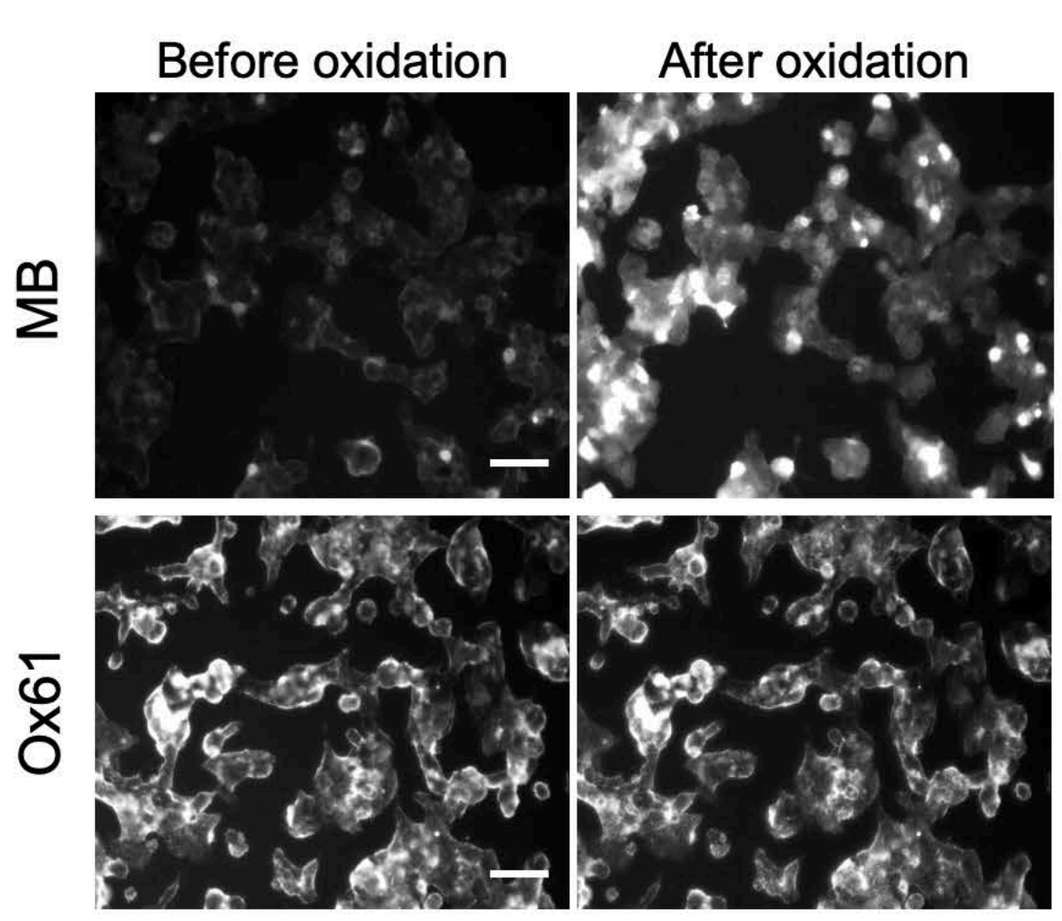

A

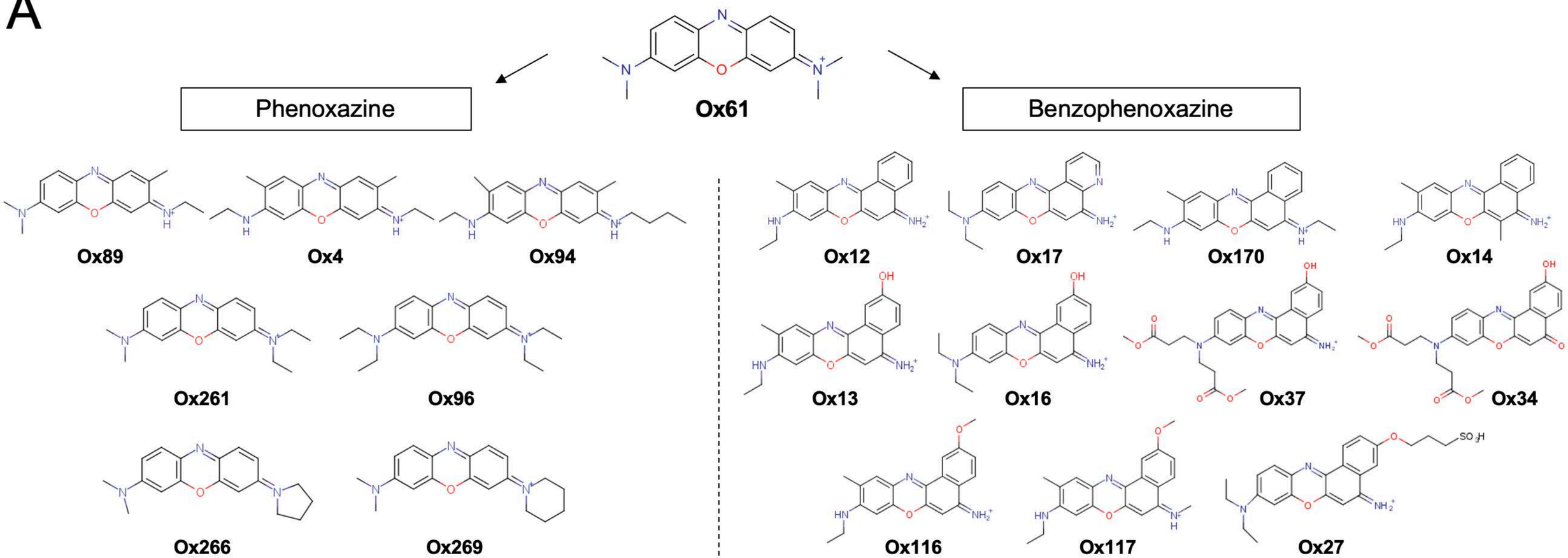
Ox61
Phenoxazine
Benzophenoxazine
Ox89
Ox4
Ox94
Ox261
Ox96
Ox266
Ox269
Ox12
Ox17
Ox170
Ox14
Ox13
Ox16
Ox37
Ox34
Ox116
Ox117
Ox27

B

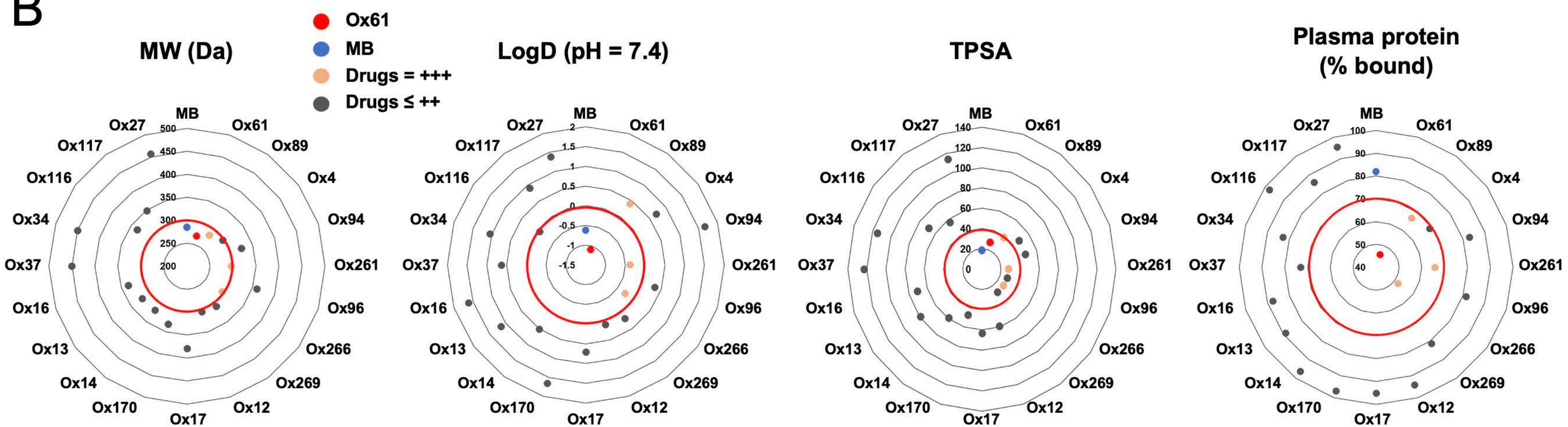
Ox61
MB
Drugs = +++
Drugs ≤ ++
MW (Da)
LogD (pH = 7.4)
TPSA
Plasma protein
(% bound)
MB
Ox61
Ox89
Ox4
Ox94
Ox261
Ox96
Ox266
Ox269
Ox12
Ox17
Ox170
Ox14
Ox13
Ox16
Ox37
Ox34
Ox116
Ox117
Ox27

A

Blood half-life	MB (min)	Ox61 (min)
$t_{1/2}\alpha$	0.43	0.73
$t_{1/2}\beta$	15.44	46.61

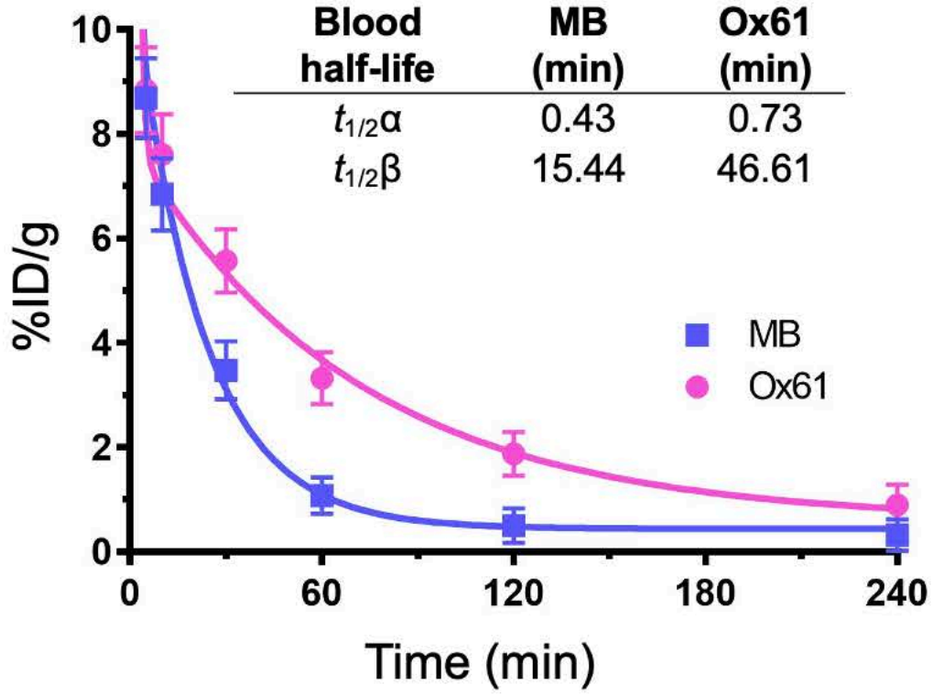

B

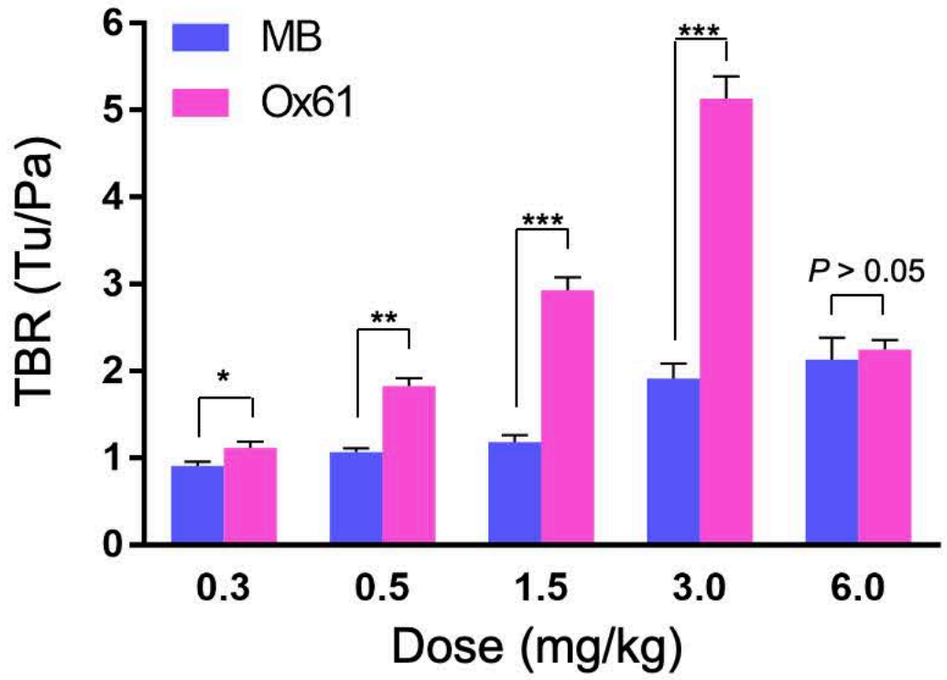

C

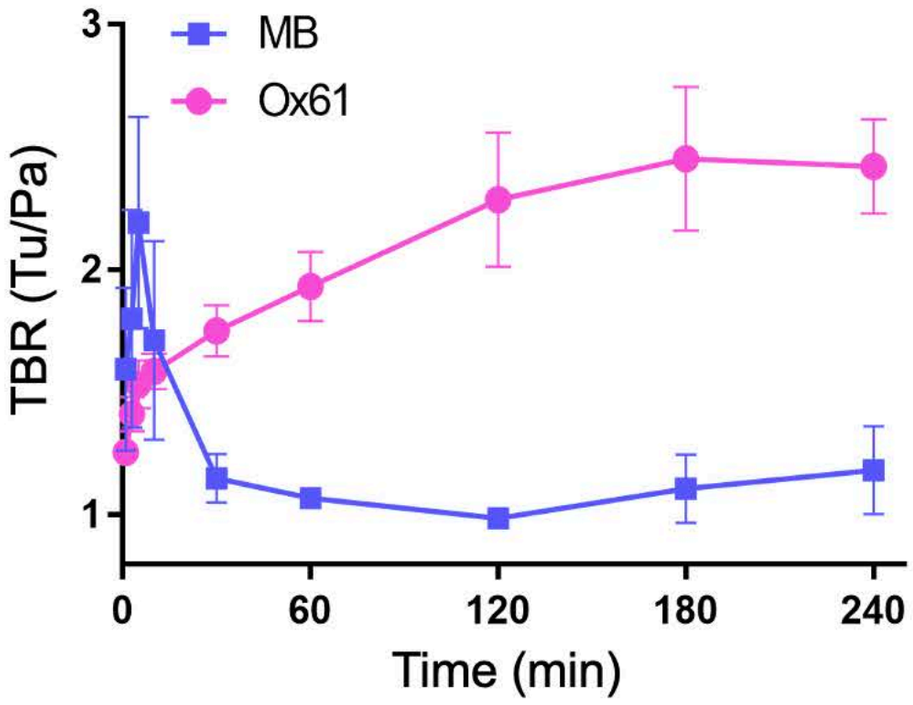

D

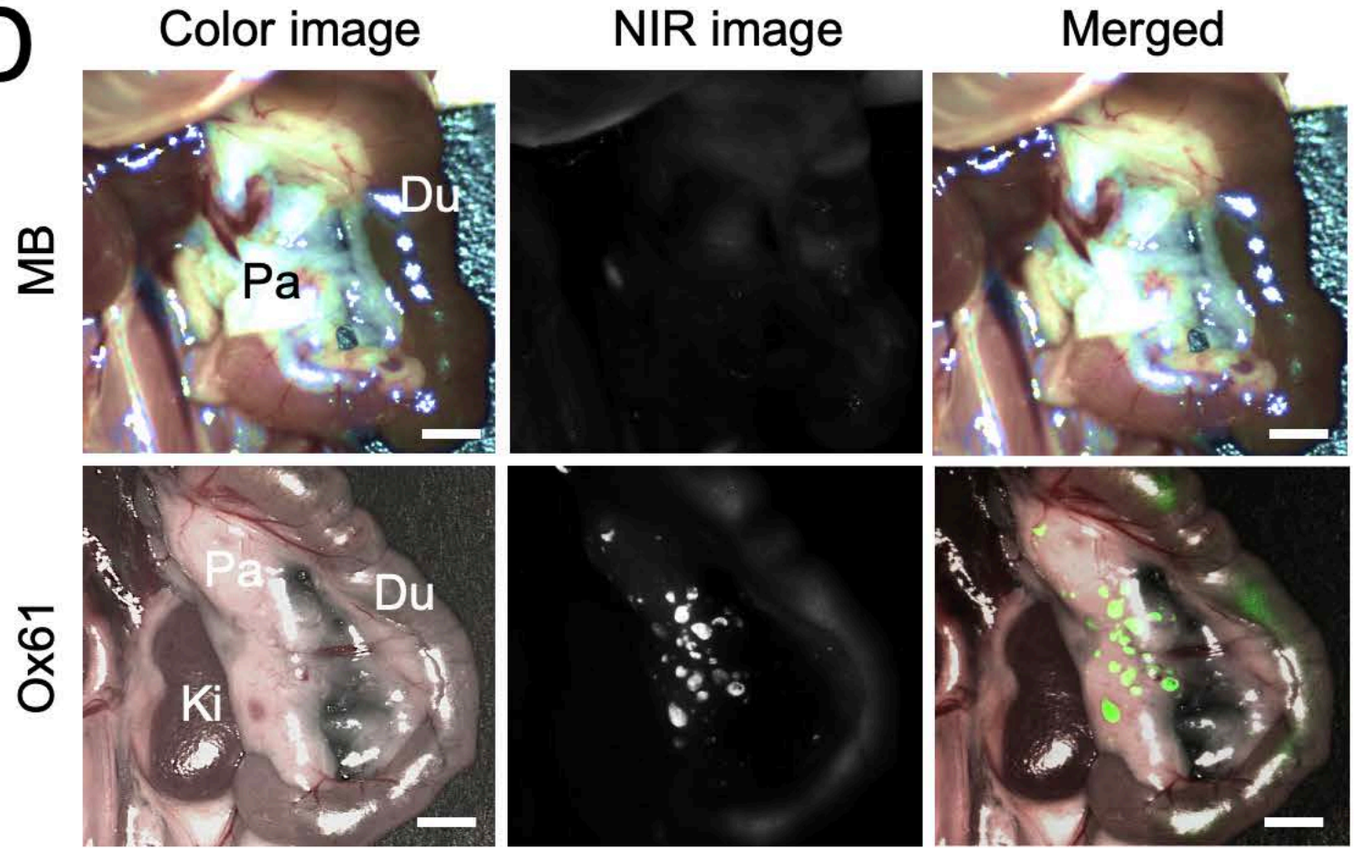

E

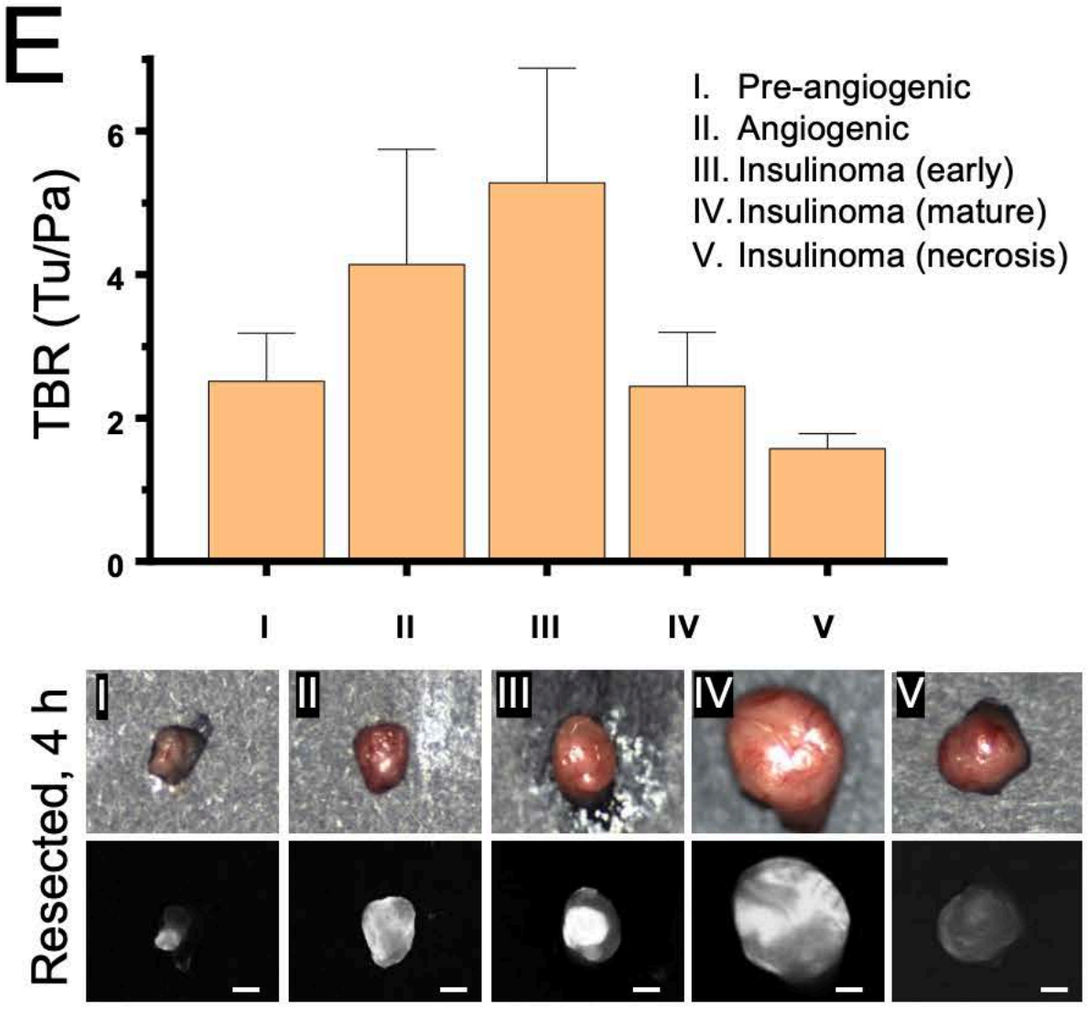

F

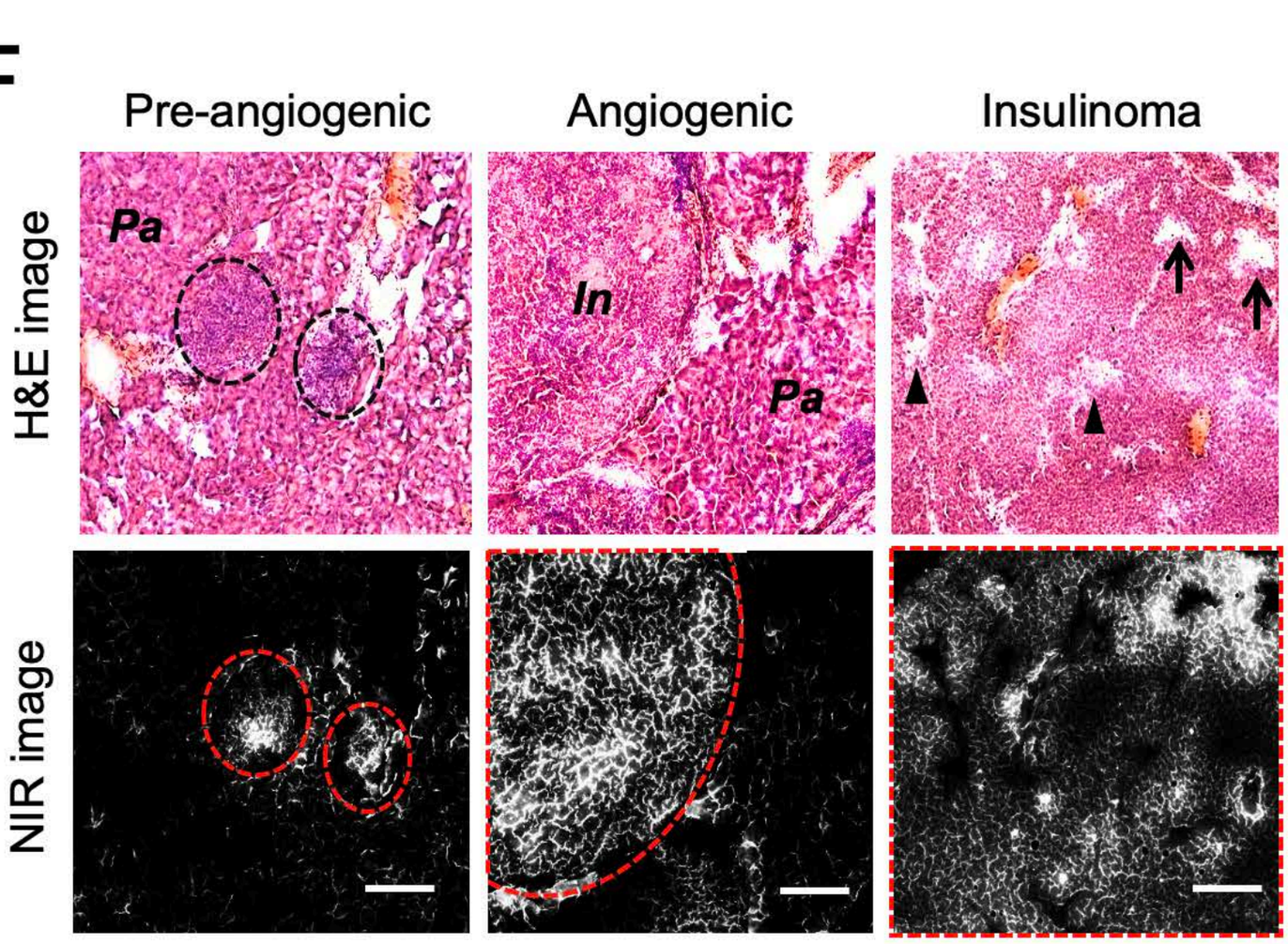

A

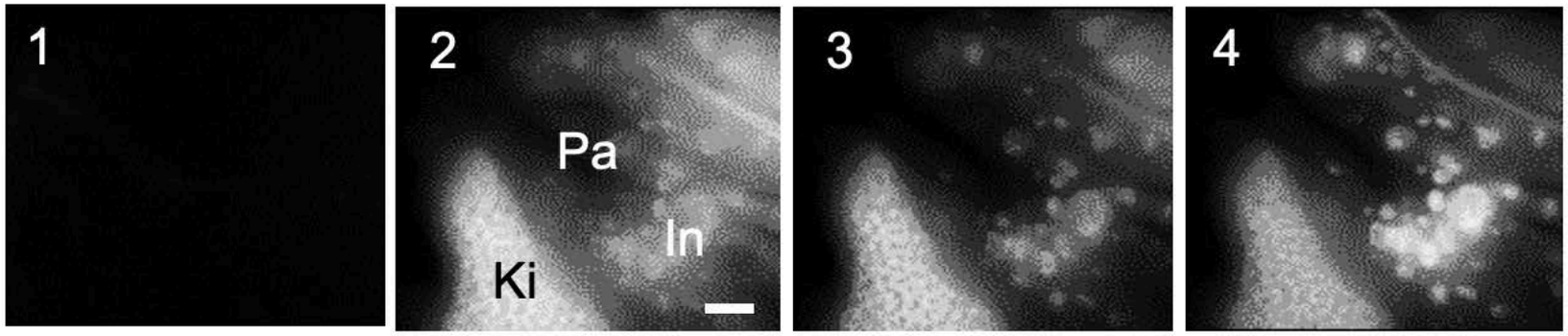
1
2
Pa
In
Ki
3
4

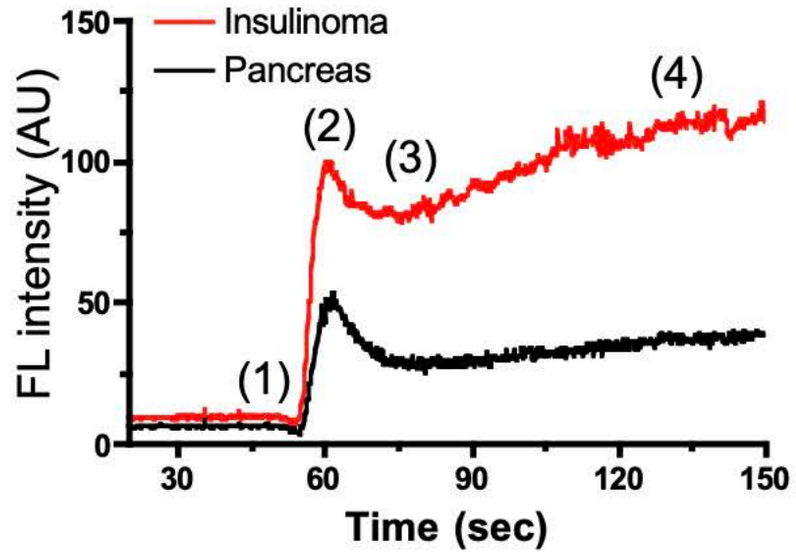
Insulinoma
Pancreas
FL intensity (AU)
150
100
50
0
(1)
(2)
(3)
(4)
30
60
90
120
150
Time (sec)

B

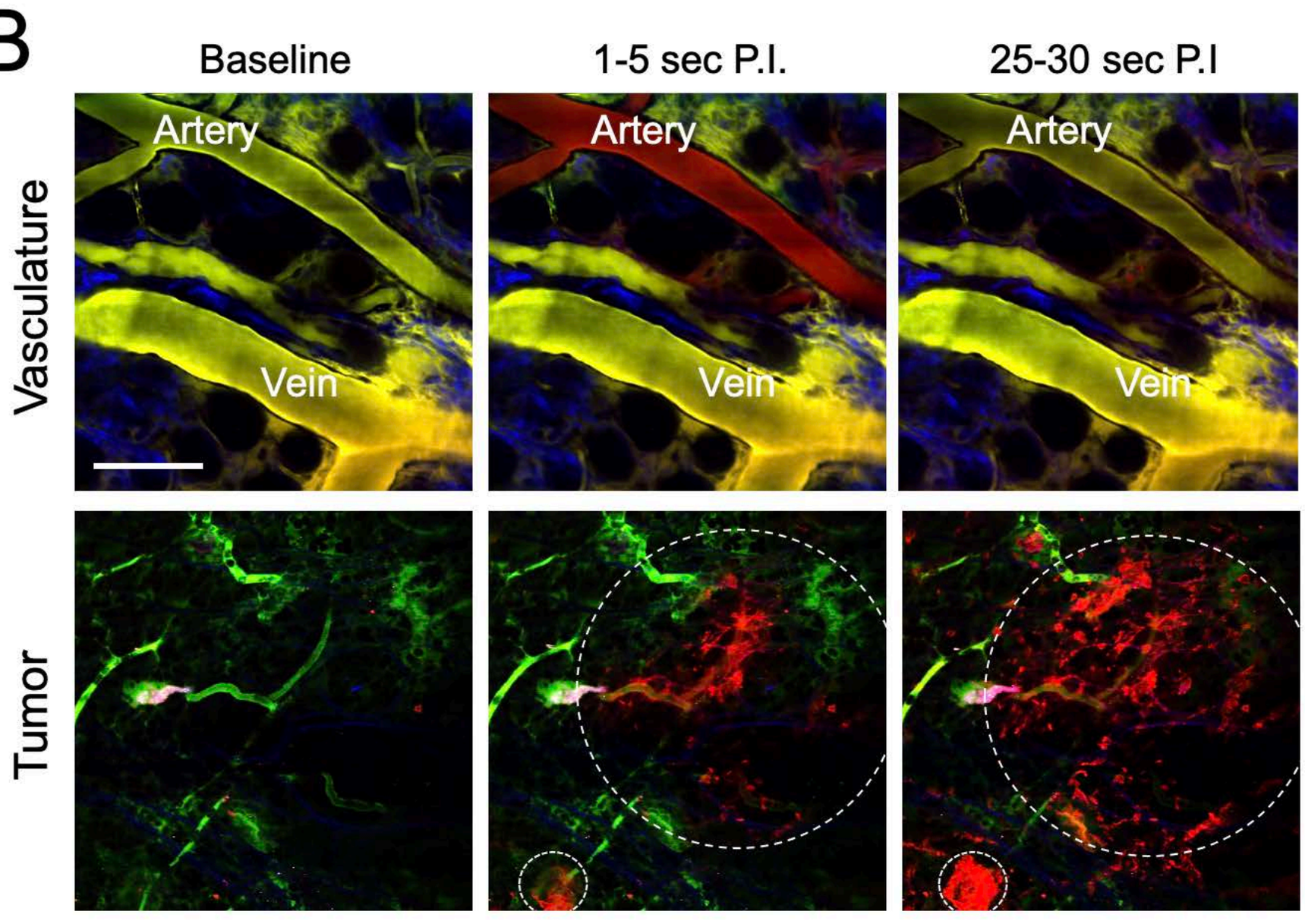
Baseline
1-5 sec P.I.
25-30 sec P.I
Vasculature
Tumor
Artery
Vein

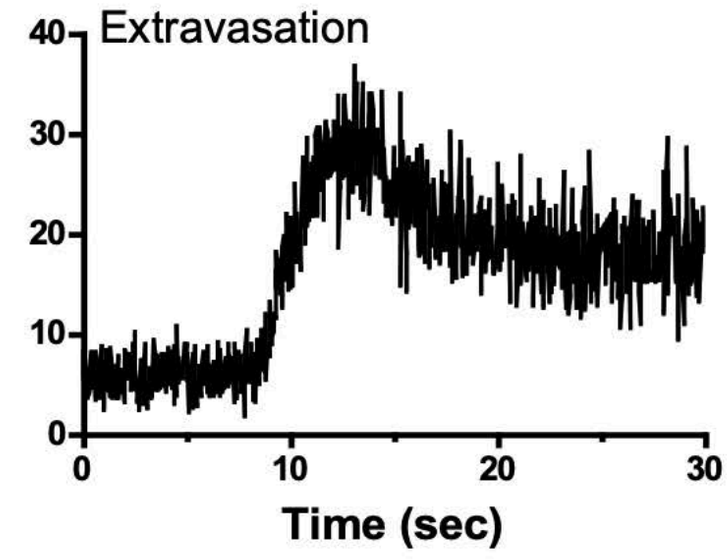
Extravasation
40
30
20
10
0
0
10
20
30
Time (sec)

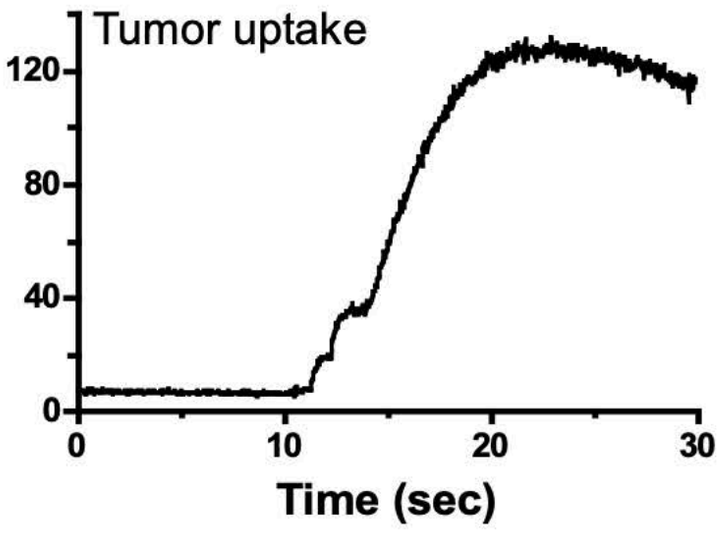
Tumor uptake
120
80
40
0
0
10
20
30
Time (sec)

Highlights

- Bioengineered near-infrared fluorescent small molecules for PNET imaging
- Highlight tumors within a minute after a single bolus injection with improved retention
- Sensitive and specific detection of ultrasmall ectopic tumors
- Intraoperative image-guided navigation provides a surgical margin